

Copyright
by
Alexander Scot Miller
2015

**The Thesis Committee for Alexander Scot Miller
Certifies that this is the approved version of the following thesis:**

**Data Driven Analysis of Fast Oxide Ion Diffusion in Solid Oxide Fuel
Cell Cathodes**

**APPROVED BY
SUPERVISING COMMITTEE:**

Supervisor:

Nicole A. Benedek

Guihua Yu

**Data Driven Analysis of Fast Oxide Ion Diffusion in Solid Oxide Fuel
Cell Cathodes**

by

Alexander Scot Miller, B.A.

Thesis

Presented to the Faculty of the Graduate School of

The University of Texas at Austin

in Partial Fulfillment

of the Requirements

for the Degree of

Master of Science In Engineering

The University of Texas at Austin

August 2015

Abstract

Data Driven Analysis of Fast Oxide Ion Diffusion in Solid Oxide Fuel Cell Cathodes

Alexander Scot Miller, M.S.E.

The University of Texas at Austin, 2015

Supervisor: Nicole A. Benedek

The goal of this study was to determine whether atomic-scale features (related to composition and crystal structure) of perovskite and perovskite-related materials could be used to predict fast oxide ion diffusion for Solid Oxide Fuel Cell (SOFC) applications; materials that can be used as SOFC cathodes were a particular focus. One hundred and twenty six pairs of diffusion (D^*) and surface exchange (k^*) coefficients for a variety of materials were collected from literature sources published between 1991 and 2015. A website was created with these data for public viewing. Statistical tests revealed that diffusion measurements have significant differences at 400K, 700K, and 1000K when grouped according to material family and sample type. Models predicting diffusion rates were created from atomic-scale features at several temperatures between 400K and 1000K. Perovskite and double-perovskite models explained >85% of the variance in

$\ln(D^*k^*)$ at 800K-1000K, meaning these models successfully predicted $\ln(D^*k^*)$ more than 85% of the time. These models explained 55%-75% of the variance at lower temperatures (400K-700K). Materials whose B-site cations had the highest electron affinities showed the fastest diffusion at all temperatures. Thus, these models suggest using B-site cations with high electron affinities (i.e. atoms that are easily reduced) may increase fuel cell performance, even at low and intermediate temperatures.

Table of Contents

List of Tables	viii
List of Figures	ix
Chapter 1: Introduction	1
1.1 Solid Oxide Fuel Cells	2
1.2 Materials For SOFC Cathodes	5
1.3 Cathode Performance	9
1.3.1 Oxygen Migration	10
1.3.2 Vacancy Formation and Migration	12
1.5 Measurement Type.....	13
Chapter 2: Methods.....	15
2.1 Data Collection	15
2.2 Statistical Analysis and Modeling Techniques	16
2.2.1 Analysis of Variance (ANOVA).....	16
2.2.2 Regression	17
2.2.3 Regularization	18

2.2.4 Feature Selection.....	19
2.2.5 Cross Validation.....	21
2.2.6 Model Assessment	22
Chapter 3: Results	24
3.1 Webpage for Data Overview	24
3.2 Differences in Categorical Variables	26
3.3 Predictive Analysis	29
3.3.1 The Initial Model	29
3.3.2 Recreating the Model at Other Temperatures	34
Chapter 4: Conclusions	38
References:	40

List of Tables

Table 1: Features used in this analysis	20
Table 2: p-values of ANOVAs corresponding to $\ln(D \cdot k^*)$	28
Table 3: Recursive Feature Elimination (RFE) results	30
Table 4: Feature projections onto the first principle component	33
Table 5: Model error at multiple temperatures.....	35

List of Figures

Figure 1: Overview of SOFC reaction using CH ₄ as a fuel	4
Figure 2: ABO ₃ cubic perovskite structure (A-cation = blue, B-cation = green, Oxygen = red)	6
Figure 3: The n = 1 Ruddlesden-Popper structure (A-cation = blue, B-cation = green, Oxygen = red)	7
Figure 4: The A-site ordered double perovskite structure (A-cation = blue, A'-cation= black, B-cation = green, Oxygen = red).....	8
Figure 5: Migration of vacancies in a curved path, through the critical triangle. 10	
Figure 6: Plot of ln(D*) and ln(k*) showing they are strongly correlated	25
Figure 7: Plot of electron affinity (B-cation) vs ln(D*) at 700K	25
Figure 8: Zooming into a plot and hovering over the data point displays information on literature reference, measurement type, sample type and material family.	26
Figure 9: Box plots of material family vs ln(D*k*) at 400K.....	27
Figure 10: Box plots of material family vs ln(D*k*) at 700K.....	27
Figure 11: Box plots of material family vs ln(D*k*) at 1000K.....	28
Figure 12: Ionic radius (B-cation) vs ln(D*k*)	31
Figure 13: Electron Affinity (B-cation) vs ln(D*k*).....	31
Figure 14: d electron count (B-cation) vs ln(D*k*)	32
Figure 15: Electron affinity vs ln(D*k*) – Perovskite and Double Perovskite ...	35
Figure 16: Variation in ln(D*k*) captured by Perovskite and Double Perovskite models	36

Chapter 1: Introduction

Machine learning and data science are emerging as new ways to solve numerical, data-intensive problems. From analyzing telescopic data that contains more information than the entire Internet [1] to real time processing of environmental data in self-driving cars [2], the applications of machine learning and data science are far reaching. Given enough data and a set of rules based on probability and statistics, a machine can be trained to predict future outcomes without needing explicit programming instructions.

Recently, statistical methods and data mining have been applied to materials science with success. Gaultois et. al. used the existing scientific literature to mine data (electrical resistivity, thermal conductivity, elemental scarcity, number of atoms per unit cell, etc.) on thermoelectric materials, which use a temperature gradient to produce an electric potential (or vice versa). The authors published an interactive web page¹ that could be used to highlight relationships between different physical parameters. [3] Their goal was to allow readers to visualize relationships in the data, potentially uncovering new and interesting correlations for further exploration of thermoelectrics. Balachandran and Rondinelli applied statistical correlations to group theory techniques and evaluated the relationship between particular structural distortions (so-called ‘octahedral rotations’) and electronic charge ordering in perovskites. [4] The results can be used to better predict

¹ <http://www.mrl.ucsb.edu:8080/datamine/thermoelectric.jsp>

charge ordering (a fascinating but poorly understood phenomenon) in future studies on perovskites. Many research areas within materials science could benefit from searchable data structures containing published data spanning back to inception of the field. These databases could show unexplored relationships within the data and might incite new research directions.

A prototype of such a data structure has been constructed here. Oxide ion diffusion data pertaining to perovskite and perovskite-related SOFC cathode materials were collected from experimental literature sources. One hundred and twenty six data points have been published in an interactive web page². The diffusion data may be viewed along with five quantitative descriptor features, e.g. atomic radius and electronegativity, and sorted with three categorical features (material family, sample type, and measurement type). A detailed statistical analysis was also performed with a larger feature set to determine which feature (or features) best predicts fast oxide ion diffusion.

1.1 SOLID OXIDE FUEL CELLS

Our need for viable, cleaner energy sources is nothing new. Coal and gas remain the most economically viable options (3-5 and 2-4 c/kWh, respectively [5]) for stationary power generation. Wind is similarly inexpensive per unit of energy output (3-5 c/kWh [5]), but requires much more land area than a traditional power plant and is subject to large cost fluctuations throughout the supply chain. [6]

² <http://tinyurl.com/p82vdbs>

Fuel cells are a promising alternative to the aforementioned energy sources, offering high efficiency (up to 63% for Solid Oxide Fuel Cells [9]) and low greenhouse gas emissions. Fuel cells have already found commercial applications; Bloom Energy is utilizing stationary fuel cell arrays to create distributed power networks that provide energy nearer to the sites of demand. [51] One especially useful fuel cell application is for data centers, which require tremendous amounts of electricity and must be located near a major power source. [52]

Fuel cells can also find use in automobiles. Transportation of people and goods comprises 28% of all U.S. energy; 86% of this energy comes from fossil fuels. [7] Although electric vehicles are becoming more popular, their reliance on externally produced energy, e.g. from a power plant, does not necessarily result in lower fossil fuel consumption overall. One way to curb emissions on a larger scale is to design a smarter grid system that better utilizes energy during off-peak hours. [8] A second way might be to supplement (or replace) the internal combustion engine with a fuel cell.

Fuel cells are devices that convert chemical energy (from a fuel) into electrical energy, waste gas, and water. [10] A fuel cell's components are in principle the same as those of a battery: two electrodes are separated by an electrolyte. Fuel cells do not require combustion of the fuel, making them efficient and environmentally friendly. [9, 11] The fuel combines with oxygen gas from air and generates electricity from a chemical reaction, much like a battery. Unlike a battery, the fuel cell does not require recharging and will produce energy as long as fuel is supplied. [10]

The type of fuel cell studied here is the Solid Oxide Fuel Cell (Figure 1 [13]), which uses a solid ceramic material as the electrolyte. As with other fuel cells, SOFCs operate purely on hydrogen. Unlike other fuel cells, SOFCs can also utilize hydrocarbon fuels, which are internally converted into H_2 . [12] Oxygen is reduced on the cathode surface and then migrates down a concentration gradient through the electrolyte and into the anode where it is oxidized. The electrons produced in this oxidation move through a conductor (producing current) and rejoin the cathode where the cycle repeats.

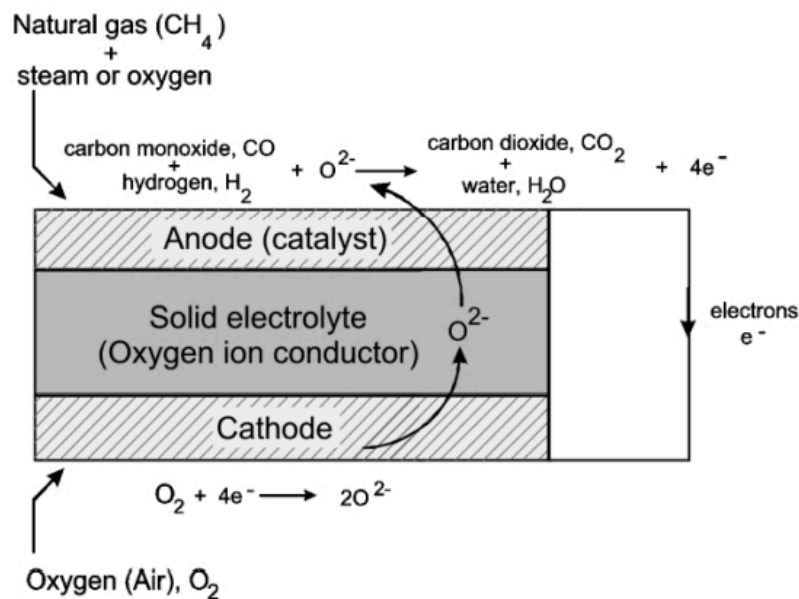


Figure 1: Overview of SOFC reaction using CH_4 as a fuel

To avoid power losses, SOFCs traditionally operate at high temperatures (near 1300K). However, continuous operation at high temperatures ultimately leads to

mechanical problems. [11] While these can be overcome to some degree in stationary applications, the problems are exacerbated in automobiles. [14] A move to lower temperatures (700K-1000K) would, for example, lower the corrosion rate of metallic components and reduce start-up and shut-down times. [14]

This report will focus on the ionic transport properties of SOFC cathode materials. Mixed ionic-electronic conducting (MIEC) materials will be the focus of this report. MIEC materials are especially useful in SOFC cathodes, as they conduct both electrons and oxide ions (in contrast to conventional cathodes, which are only electronically conducting). If the cathode is made of a MIEC material, the full surface area can be utilized for catalysis of the oxygen reduction reaction (ORR) and oxide diffusion can occur throughout the entire material. Thus, cathodes made from MIEC materials may exhibit faster ion diffusion at lower temperatures than conventional cathodes. However, both the ORR and bulk diffusion are thermally activated processes and are intrinsically slower at low temperatures for all materials. A major goal in SOFC research is to find cathode materials that exhibit fast oxide diffusion at low or intermediate temperatures.

1.2 MATERIALS FOR SOFC CATHODES

Perhaps the most extensively investigated material family for SOFC cathodes has been the perovskite family, whose materials have shown promise in commercial applications. [10] Layered perovskite materials (especially Ruddlesden-Popper and ordered double perovskite families) are also being studied for use as cathode materials.

Research suggests these anisotropic layered materials may on average exhibit faster ion transport at intermediate temperatures than conventional perovskites [15, 27, 31, 53]. All three families contain MIEC materials, although Ruddlesden-Popper phases and double perovskites have been more extensively investigated for their MIEC properties.

Perovskites (Figure 2) are ceramic materials with chemical formula ABO_3 where A is typically a rare earth or alkaline earth element and B is a transition metal. Given the large number of compositional combinations (almost every element of the periodic table can substitute at the A or B site [63]), the perovskite family is, both structurally and chemically, very versatile.

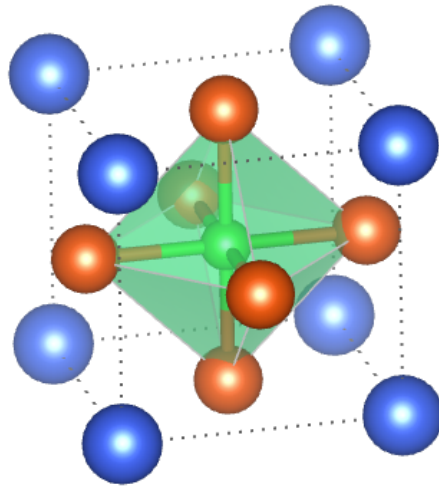


Figure 2: ABO_3 cubic perovskite structure (A-cation = blue, B-cation = green, Oxygen = red)

Ruddlesden-Popper phases form a homologous series and are comprised of n ABO_3 blocks between sets of two AO rocksalt layers (Figure 3), with the chemical

formula $A_{(n+1)}B_nO_{(3n+1)}$. [15]. As with bulk perovskites, the A-site cations are typically lanthanides or alkaline earth metals, while B-site cations are transition metals. Excess oxygen has been shown to readily incorporate between the AO rocksalt layers of $n=1$ Ruddlesden-Popper nickelates $A_2NiO_{4+\delta}$ ($A = La, Pr, Nd$). [28, 64, 65] The excess oxide ions migrate through an interstitialcy mechanism with a low activation barrier, resulting in fast ionic transport in these nickelates. [29]

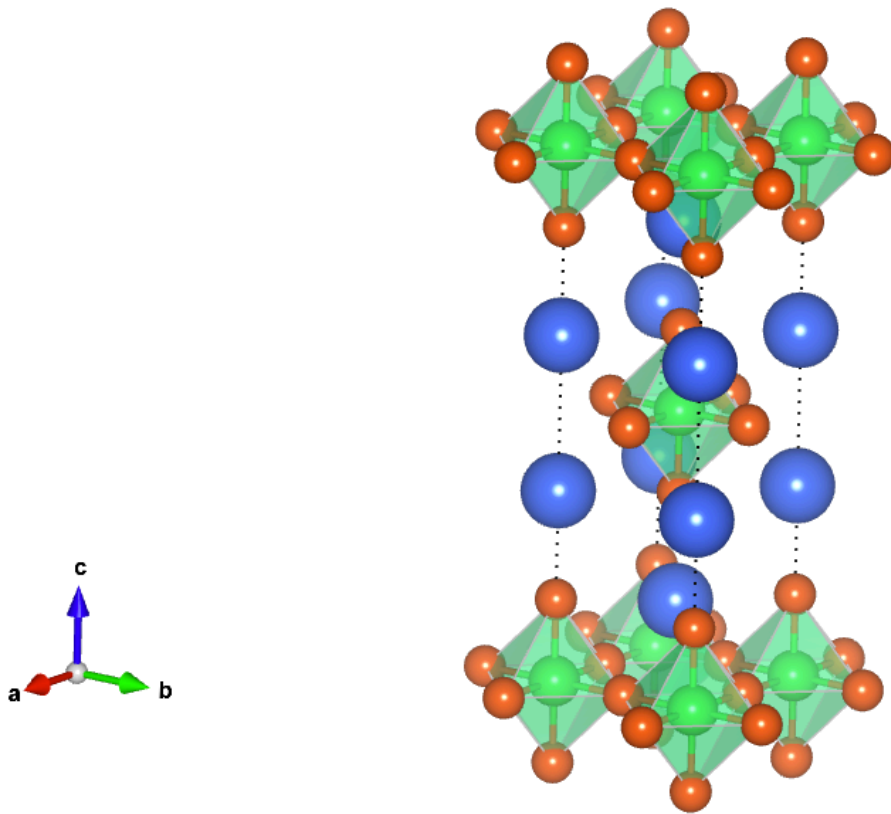


Figure 3: The $n = 1$ Ruddlesden-Popper structure (A-cation = blue, B-cation = green, Oxygen = red)

Double Perovskites have the chemical formula of $AA'B_2O_{(5+x)}$, where (in the materials being considered for SOFC cathodes) A is typically a rare earth metal, A' is an alkaline earth metal, and B is a transition metal. The subset of particular interest for SOFC cathodes is comprised of materials in which the A- and A'-cations order in alternating (0 0 1) layers, where the [001] direction is parallel with the c axis in Figure 4.

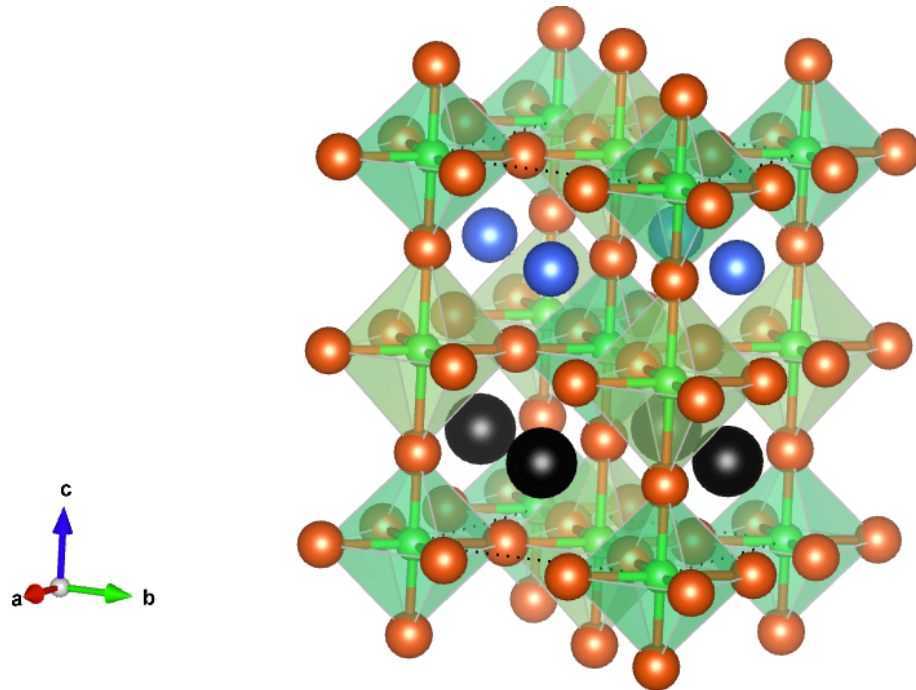


Figure 4: The A-site ordered double perovskite structure (A-cation = blue, A'-cation= black, B-cation = green, Oxygen = red)

In contrast to the nickelate RP phases, oxide ion diffusion occurs in double perovskites by a vacancy mechanism. [30, 31] Oxygen vacancies form primarily in the A'-cation layers. [30] Faster diffusion has been observed when the A and A' cations are

fully ordered in layers. [15, 22, 37, 38] Furthermore, double perovskites show a much faster rate of oxygen uptake (with respect to ABO_3 perovskites), which is the rate-limiting step for many cathode materials. [30]

1.3 CATHODE PERFORMANCE

MIEC cathodes require both good catalytic activity on the surface (for the ORR) and fast ion diffusion through the material. These two processes may be captured by two kinetic rate coefficients that both obey Arrhenius behavior and are therefore thermally activated: surface exchange (k) and bulk diffusion (D). [16] It is desirable for both coefficients to be large at temperatures of interest, which here are between 400K-1000K: the low-intermediate temperature regime [66]. It should be noted that D , k and D^* , k^* are often used interchangeably.

Although D^* and k^* are separate measurements (see Section 1.5), overall diffusion depends on both of them. Therefore, a combined D^*k^* coefficient (the product of the two individual coefficients), is frequently used to measure overall diffusion. Because the coefficients follow Arrhenius behavior, it is helpful to represent them in logarithmic form. It is important to note that while large values of D^* and k^* mean faster diffusion, they are always <1 and therefore their exponents (and logarithms) are negative; smaller values of $\ln(D^*k^*)$ thus represent faster diffusion.

1.3.1 Oxygen Migration

Surface exchange involves the oxygen reduction reaction (ORR), a multi-step surface reaction whose exact pathway is not conclusively known. [61, 31] Because the ORR happens on the cathode surface, it depends only on the first few layers of atoms. [43] Once incorporated into the cathode, oxide ions diffuse down a concentration gradient through the electrolyte and into the anode. Previous studies [18, 55, 56] found that vacancy-assisted oxide diffusion in bulk perovskites occurs along the octahedral edge in a curved path (Figure 5 [56]). In Figure 5 A^* , A'^* , O^* denote the two A-site cations and the oxygen involved in the transition state. O_{eq} and O_p are oxygen atoms not involved in the transition state. They are in planes perpendicular and parallel, respectively, to the tangent of the migration path.

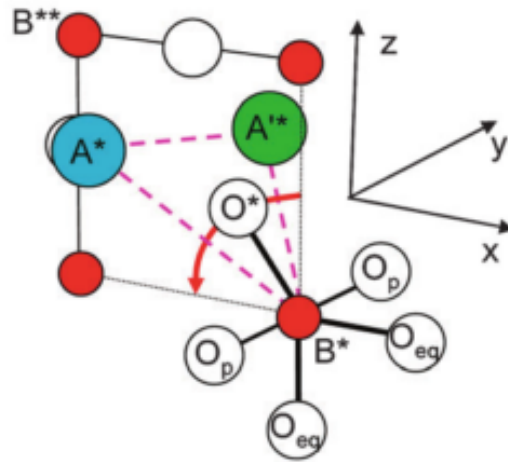


Figure 5: Migration of vacancies in a curved path, through the critical triangle

To migrate, the oxide ion must pass through two A-site cations and one B-site cation, which together form a ‘critical triangle’ [18] (Figure 5). Using the critical triangle concept, Cherry et. al. postulated that the radii of both cations affected the overall migration energy. [20] Across a series of five perovskites, A-site radius showed a positive correlation with ion migration activation energy, meaning larger cations showed slower vacancy migration. B-site radius showed an overall negative trend. Neither trend was monotonic. [20]

Ionic radii can be used to calculate the Goldschmidt tolerance factor t , [21] which is often utilized as a rough guideline to indicate structural stability of the perovskite crystal structure. It is calculated as:

$$t = \frac{r_A + r_O}{\sqrt{2} * (r_B + r_O)}$$

where r_A is A-cation radius, r_B is B-cation radius, and r_O is the radius of the oxide ion. For a perfectly stable cubic perovskite structure, $t=1$. When $t<1$, the A-site is underbonded and a BO_6 octahedral rotation distortion occurs to increase stability; this shortens the A-O bond length and optimizes the A-site coordination environment. When $t>1$, the B-site is not optimally coordinated and a ferroelectric distortion occurs whereby the B-cation moves away from the center of the octahedral cage. The tolerance factor can be related to the critical radius [25], i.e. the radius of a sphere that fits perfectly inside the critical triangle, defined as:

$$r_{critical} = \frac{r_A^2 + \frac{3a}{4} * r_B^2}{2r_A + a\sqrt{2} - 2r_B}$$

where a is the lattice parameter. This can be rewritten in terms of r_A , r_B , and r_O if the tolerance factor is not equal to one³ [26]:

$$t > 1; r_{critical} = -\frac{r_B}{2} + \frac{r_O}{2} + \frac{0.5 * (r_A + r_O)^2}{4r_A - 2r_B + 2r_O}$$

$$t < 1; r_{critical} = \sqrt{2} * r_B - r_O - (2 + \sqrt{2}) * r_A + \frac{(3 + \sqrt{2}) * (r_A + r_O)^2}{2r_A + (2r_A + (\sqrt{2} - 2) * r_B + \sqrt{2}r_O)}$$

It has been suggested [25] that both tolerance factor and critical radius are strong indicators of ion migration rate.

1.3.2 Vacancy Formation and Migration

In perovskites and double perovskites, oxide diffusion occurs by a vacancy mechanism. Oxygen vacancies form when the A-site is doped with an aliovalent ion. [19, 57] The barrier to ion migration is affected by both electronic and geometric factors. When an oxygen atom is removed from the octahedron, most of its negative charge is transferred to the neighboring B-site cations and a vacancy is created. [23] Fast ion diffusion may therefore depend on the B-site cation being readily reducible. Electron affinity measures the amount of energy released from a species when it gains an electron. [24] If an atom releases energy upon reduction, the thermodynamics are such that it is

³ Such an equation cannot be written for $t = 1$ for algebraic reasons. No materials with $t=1$ were encountered in this analysis so lattice parameters were not needed.

favorable for a vacancy to form. Thus, one would expect B-site cation atoms with larger electron affinities to correlate with faster oxide ion diffusion in perovskites.

1.5 MEASUREMENT TYPE

Oxide tracer diffusion (D^*) is the proportionality constant from Fick's first law:

$$j^* = -D^* \frac{\partial C^*}{\partial x} = -D^* C_o \frac{\partial n^*}{\partial x}$$

where C_o is the concentration of oxygen atoms, x is a distance along the measurement axis, and n^* is the fraction of the tracer isotope. [68] Surface exchange is defined with a similar equation:

$$j^* = k^* C_o (n_g^* - n_s^*)$$

where n_g^* is the isotope fraction in the gas and n_s^* is the isotope fraction on the surface of the solid. [42] The two most common techniques for measuring D^* and k^* are isotope exchange depth profiling (IDEP) coupled with secondary ion mass spectroscopy (SIMS) and electrical conductivity relaxation (ECR).

In IDEP, purified $^{18}\text{O}_2$ gas is introduced into the sample environment (filled with air) and let sit for a period of time. SIMS then measures how far the isotopic gas has travelled and in what concentrations. Diffusion may be modeled with Fick's first law [39] and its solution may be written in terms of D and k . [40]

In ECR, a sample is first kept at a constant oxygen partial pressure ($p\text{O}_2$). Electrical conductivity is measured as a function of time immediately following an abrupt change in $p\text{O}_2$ at a constant temperature. [67] Fick's second law is fitted with the

collected data, using appropriate boundary conditions, to produce D_{chem} and k_{chem} : the chemical rate constants. [41] Thermogravimetric analysis (TGA) is needed to convert these coefficients to their tracer diffusion counterparts using an appropriate coefficient called the thermodynamic factor:

$$D_{chem} = \gamma D^* ; k_{chem} = \gamma k^*$$

where [62]:

$$\gamma = \frac{1}{2} * \frac{\partial \ln (pO_2)}{\partial \ln (C_O)}$$

Chapter 2: Methods

2.1 DATA COLLECTION

Diffusion (D^*) and surface exchange (k^*) coefficients were collected with the help of Zachary Levine⁴ from literature sources⁵ published between 1991 and 2015. In total, 126 unique data points (containing both D^* and k^*) were recorded. These coefficients were found either by extrapolation of a figure depicting an Arrhenius curve (D^* or k^* vs. $1/T$) or from a table with the exact values. Values for each of the features (Table 1) were calculated for every material based on its chemical formula.

Given the activation energy (E_a) of a material and the coefficient (D^* or k^*) at a certain temperature (T_0), the Arrhenius equation can be used to estimate the coefficient at any other temperature (T):

$$\ln(D^*) = \frac{-E_a}{R} * \frac{1000}{T} - \frac{1000}{T_0} + \ln(D_0^*)$$

$$\ln(k^*) = \frac{-E_a}{R} * \frac{1000}{T} - \frac{1000}{T_0} + \ln(k_0^*)$$

However, extrapolating far from the measured temperature will often be inaccurate due to changes in phase and stability of the material. Because a large range of

⁴ Zachary Levine, an undergraduate Mechanical Engineering researcher, helped find many of the literature sources and recorded their data points. He also calculated values for several of the feature columns in the data table.

⁵ The citation for any data point can be found on the webpage (<http://tinyurl.com/p82vdbs>) upon clicking on that data point.

temperatures (400K-1000K) was studied here, such extrapolations were necessary in some cases, e.g. for experiments conducted only above 1000K.

2.2 STATISTICAL ANALYSIS AND MODELING TECHNIQUES

2.2.1 Analysis of Variance (ANOVA)

Analysis of Variance (ANOVA) is a very common statistical technique that tests differences between means in two or more groups of measurements. Originally developed by R.A. Fischer in 1936 [47], the technique uses an F-test to compare sample means of all groups non-discriminately such that the null hypothesis is

$$\mu_1 = \mu_2 = \dots = \mu_n$$

The sums of squares (SS) are first found from variance:

$$s^2 = \sum_{i=1}^I (y_i - \langle y \rangle)^2$$

where y_i is the value of the i -th measurement and $\langle y \rangle$ is the average measurement value. Next, the sums of squares are partitioned into the sums of squares within groups and the sums of squares between groups. The degrees of freedom (DF) are partitioned in a similar way. Using these values, an F-statistic is calculated such that:

$$F = \frac{\frac{SS_{between}}{DF_{between}}}{\frac{SS_{within}}{DF_{within}}}$$

After parameterizing an appropriate probability distribution with the F-statistic [44], a p-value is obtained which may be interpreted as the probability of observing the given data provided the null hypothesis is true, i.e. that all groups' means are equal. If this value is low (typically <0.05), the null hypothesis is rejected and the result is considered statistically significant. In this event, there is strong evidence to suggest the groups are different.

In this analysis, measurements were partitioned into groups for three separate tests; the effects of material family, sample type, and measurement type were separately analyzed. For example, the material family test determined whether measurements on perovskites, double perovskites, and Ruddlesden-Popper materials showed significantly different values of $\ln(D^*k^*)$.

2.2.2 Regression

While ANOVA is a useful technique with which to begin, it often fails to answer the most important question – how can the data be used to predict future outcomes? In this analysis, models were built to explain how fast ion diffusion may be predicted from a given material's chemical formula.

Regression quantifies the effect some combination of features has on the outcome of a continuous variable, e.g. D^*k^* . Linear regression fits a model with coefficients to a linear equation:

$$y = w_1X_{.1} + w_2X_{.2} + \dots + w_mX_{.m}$$

where X is a (m,n) dimensional matrix; m is the number of features (columns) and n is the number of observations (rows). The coefficients are fit to minimize the residual sums of squares (sums of differences between observations and the linear model) such that [46]:

$$\min_w \|Xw - y\|_2^2$$

where the subscript 2 denotes the use of an L_2 norm based algorithm. An L_1 norm may also be used: [48, 49]

$$L_1: \|x\|_1 = \sum_{i=1}^n x_i \ ; \ L_2: \|x\|_2 = \sum_{k=1}^n (x_k)^2$$

The regression must fit a linear relationship between each feature in X and the outcome y . Regression may be extended to polynomial orders by creating new columns in the feature matrix that are combinations of existing columns. For example, let

$$X = \begin{vmatrix} 2 \\ 3 \end{vmatrix}$$

A third order polynomial may be fit to the data by expanding this matrix to

$$X = \begin{vmatrix} 2 & 4 & 16 \\ 3 & 9 & 81 \end{vmatrix}$$

where the additional columns represent the first column squared and cubed. Mixed order columns are included for X matrices with multiple features (columns).

2.2.3 Regularization

In general, a regularization method will penalize poorly fitting features in the overall model; a regularization parameter is added to the minimization scheme.

Ridge regularization is an algorithm that is especially useful with dense feature matrices (i.e. matrices with few 0s). [50] It can be written as an addition of L_2 regularization to the regression minimization scheme: [46]

$$\min_w \|Xw - y\|_2^2 - \alpha \|w\|_2^2$$

where α is the regularization parameter, constrained by $\alpha \geq 0$. Larger values of α translate to harsher penalties for bad features. This makes the model less susceptible to multicollinearity problems (i.e. linear relationships between features), but may affect the model's robustness. [46, 50]

2.2.4 Feature Selection

Before constructing a model, it is important to determine the best subset of features. Good feature subsets contain features that explain large amounts of variance but are not linearly related. For example, atomic radius and atomic mass would not be included together because they follow the same periodic trend and are therefore related.

A pool of 13 features was used in this analysis (Table 1). Two classes of quantitative features are shown in Table 1. One contains features related to the parent perovskite in each material. The other relates to the average values (including dopants) of the material. For example, the material $Ba_{0.8}Sr_{0.2}FeO_3$ has the parent perovskite $BaFeO_3$. Therefore, the parent A-cation radius would simply be the radius of Ba^{2+} while the average A-cation radius would be the weighted radius average: $0.8 * R(Ba^{2+}) + 0.2 * R(Sr^{2+})$.

This was an important distinction because many samples were heavily doped and it was unclear what effects these dopants had.

Feature	Description
Electron affinity (A-site, parent)	Electron affinity of the parent ion in the A-cation site
Electron affinity (B-site, parent)	Electron affinity of the parent ion in the B-cation site
Radius (A-site, parent)	Ionic radius of the parent ion in the A-cation site
Radius (B-site, parent)	Ionic radius of the parent ion in the B-cation site
d count (B-site, parent)	Number of d-shell electrons in the parent ion of the B-cation site
Electron Affinity (A-site, average)	Average electron affinity of parent and dopant ions in the A-cation site
Electron Affinity (B-site, average)	Average electron affinity of the parent and dopant ions in the B-cation site
Radius (A-site, average)	Average ionic radius of the parent and dopant ions in the A-cation site
Radius (B-site, average)	Average ionic radius of the parent and dopant ions in the B-cation site
d count (B-site, average)	Average number of d-shell electrons in parent and dopant ions in the B-cation site
Tolerance Factor	Goldschmidt tolerance factor calculated using average radius values of A- and B-site cations
Critical Radius	Critical triangle radius ($r_{critical}$) calculated using average radius values of A- and B-site cations
Material Family*	Perovskite, double perovskite, and Ruddlesden-Popper
Sample Type*	Ceramic, single crystal, and thin film
Measurement Type*	IEDP/SIMS, ECR, and EBSP

*These features were categorical (i.e. did not have numeric values)

Table 1: Features used in this analysis

Principle Component Analysis (PCA) is a way to project a set of features onto a subspace of much smaller dimension (often 2 or 3 dimensions for visualization purposes).

A covariance matrix is computed for all input dimensions and then its eigenvectors and eigenvalues are calculated. The eigenvectors represent linear combinations of feature vectors in feature space (principle components). Corresponding eigenvalues represent the proportion of total variance explained by these principle components. [60] The data may be projected onto the principle components with the highest eigenvalues for visualization. Furthermore, projections of the original features onto the principle components may be calculated to determine the relative amount of variance captured by the individual features.

Recursive Feature Elimination (RFE) may be used to determine which features individually contribute most to variance. In RFE, a regression (or any estimator that assigns weights to features) is trained on a subset of features, which shrinks during each iteration until the desired number of features is reached. [44] The features removed between iterations are the ones that contribute the least to overall variance (i.e. the features whose absolute weights are the smallest).

2.2.5 Cross Validation

In addition to choosing features and a model, it is important to ensure the data does not overfit. The goal is to generate a robust, generalizable model that can predict future data and not just trends in the data used to create it. An additional constraint makes our analysis unlike most machine learning problems: the data is relatively small (126 data points) and has few features (13), making any models susceptible to overfitting. In order

to assess whether our model is producing statistically meaningful predictions, it is important to utilize the machine learning concept of cross-validation.

In basic supervised learning, the model is optimized on a set of training data and then evaluated on a separate set of test data. This can be insufficient because:

- The data set may not be large enough to significantly populate both training and test subsets.
- Model performance is evaluated on the test set, which means the model is optimized to fit that set of data. This does not always translate to a generalizable model.

Cross validation alleviates these issues by creating another partition of data on which the model is optimized before assessing performance on the test set.

Leave-One-Out cross-validation removes one data point from the data set. The remaining $m-1$ data points are fitted to a model, which is then tested with the data point that was left out. This procedure is repeated m times and the results are averaged. [46] Any number of data points can be left out (termed 'leave- p -out' for $p>1$), but leave-one-out is ideal for small data sets such as the one in this analysis.

2.2.6 Model Assessment

Models are assessed by how much error is present and by how much variance they explain with respect to the observed measurements.

Mean Squared Error (MSE) shows the difference between the model and what was observed. It is especially useful in comparing models: [58]

$$MSE = \sum_{i=1}^n (Y_{i,model} - Y_{i,observed})^2$$

R^2 (coefficient of determination) determines a model's goodness of fit. Many varieties exist, but the basic coefficient is interpreted as the proportion of total variance explained by the model: [59]

$$R^2 = 1 - \frac{\sum_{i=1}^n (y_{i,observed} - y_{i,model})^2}{\sum_{i=1}^n (y_{i,observed} - \langle y_{i,observed} \rangle)^2}$$

Chapter 3: Results

The data were explored visually by constructing a web page using d3 and jQuery Javascript libraries. Single factor ANOVA tests were then performed on material family, sample type, and measurement type using the Python package SciPy. [44] A longer quantitative data analysis was performed using two Python packages: Pandas [45] (for loading and manipulating the data) and SciKit-Learn [46] (for the machine learning/statistical algorithms). In this analysis, models were fit to predict D^*k^* from subsets of 13 total features (Table 1).

3.1 WEBPAGE FOR DATA OVERVIEW

The interactive webpage (Figures 6-8) can be accessed at <http://tinyurl.com/p82vdbs>. It is freely hosted thanks to GitHub.com and bl.ocks.org. Data is plotted on two axes of the user's choosing and a slider bar at the top of the page may be used to control temperature. Data may be sorted by any combination of material family, sample type, and measurement type using links at the top of the page. The scatter plots are zoomable and scrollable. Information on each individual data point appears when the user hovers over it. Upon clicking on a data point, the user is redirected to a DOI reference of the citation.

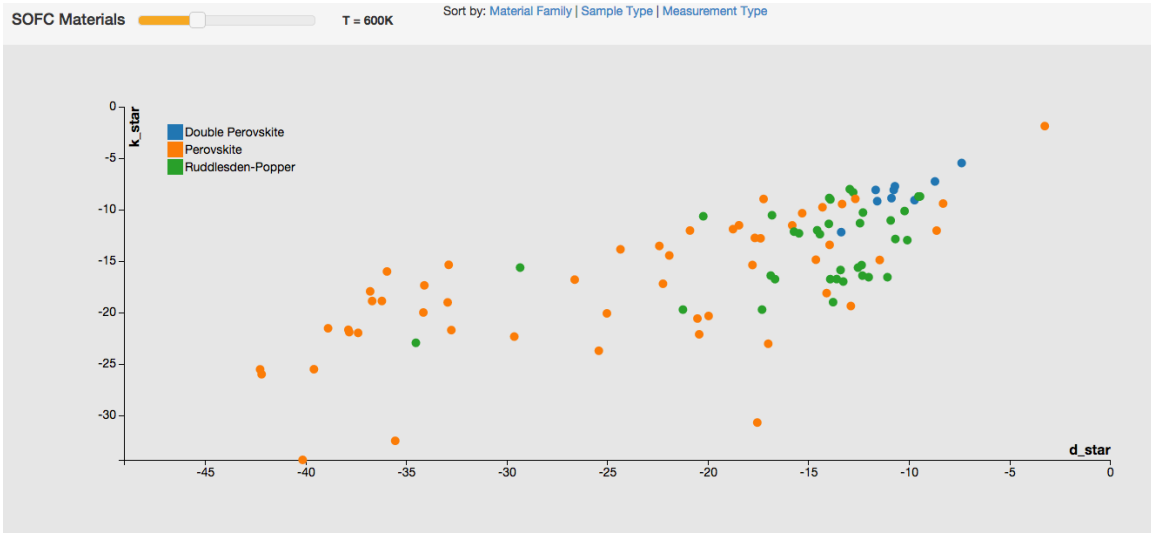


Figure 6: Plot of $\ln(D^*)$ and $\ln(k^*)$ showing they are strongly correlated

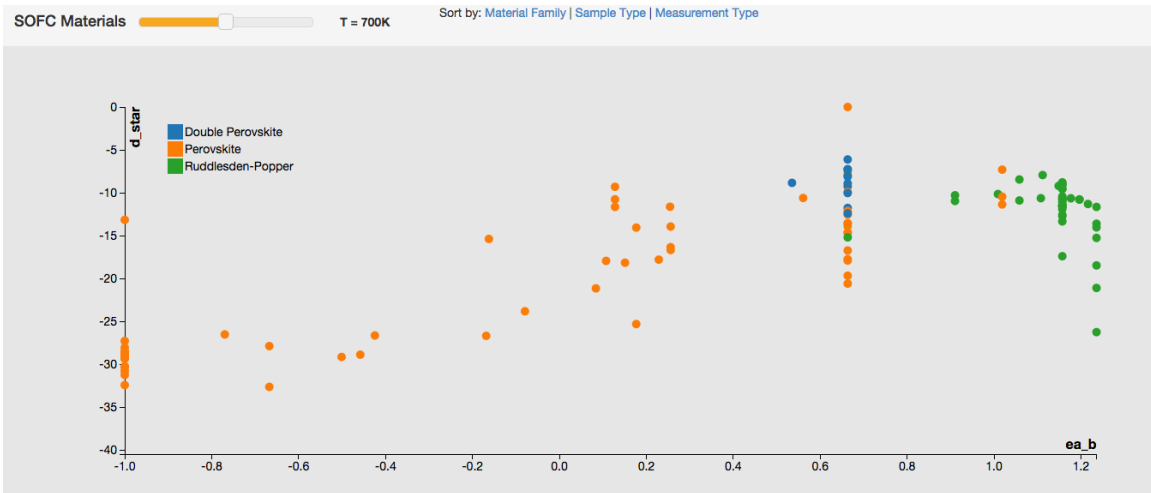


Figure 7: Plot of electron affinity (B-cation) vs $\ln(D^*)$ at 700K

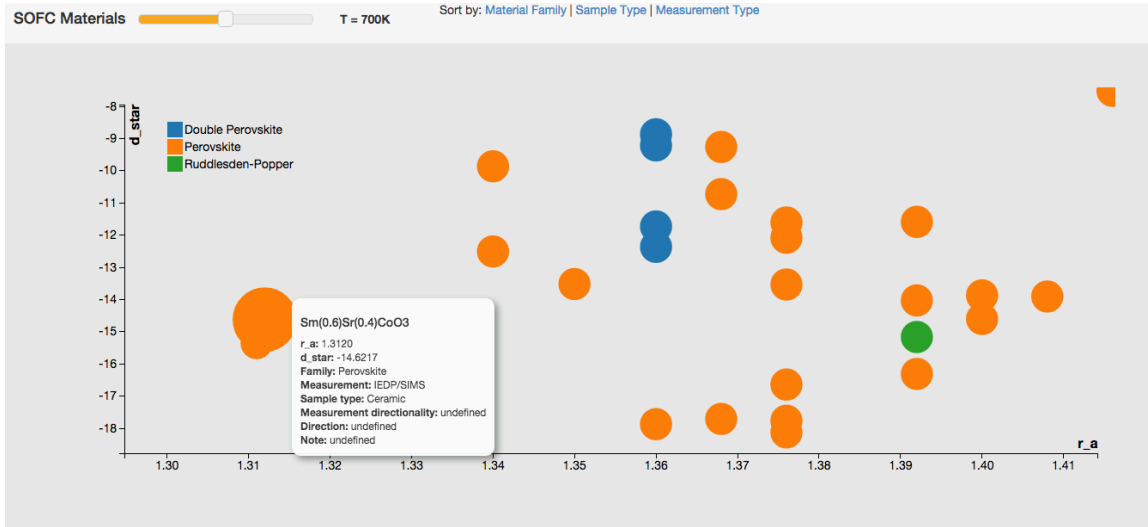


Figure 8: Zooming into a plot and hovering over the data point displays information on literature reference, measurement type, sample type and material family.

3.2 DIFFERENCES IN CATEGORICAL VARIABLES

Because the primary focus of this study was the materials themselves, box plots were drawn (Figures 9-11) to visually inspect how $\ln(D^*k^*)$ varied for different material families. At all three temperatures (400K, 700K, and 1000K) perovskite materials showed the slowest diffusion (largest $\ln(D^*k^*)$) and double perovskites showed the fastest diffusion.⁶ Relative differences in these subgroups were smaller at higher temperatures, but visible differences were present at all three temperatures. The range of

⁶ Again it is important to note that for $\ln(D^*k^*)$, *smaller* values indicate faster diffusion; conversely, individual coefficients with larger values (i.e. less negative exponents) indicate faster diffusion.

diffusion for perovskites was much larger than for either layered perovskite family because there was much more data on perovskites.

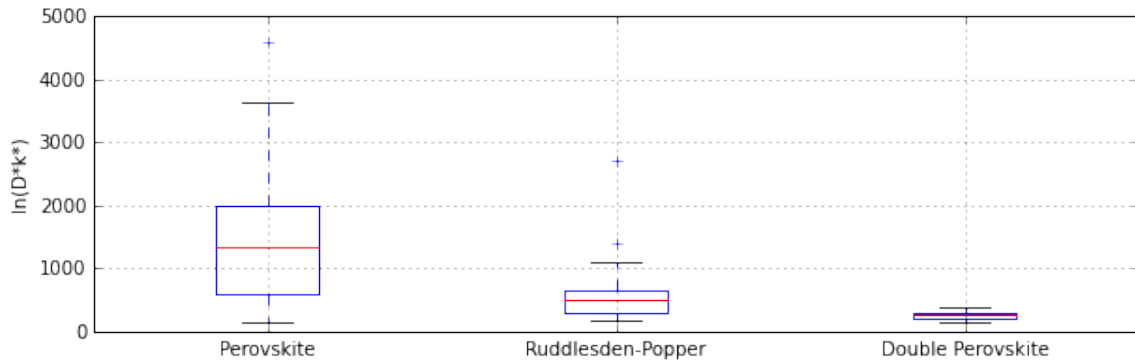


Figure 9: Box plots of material family vs $\ln(D \cdot k^*)$ at 400K

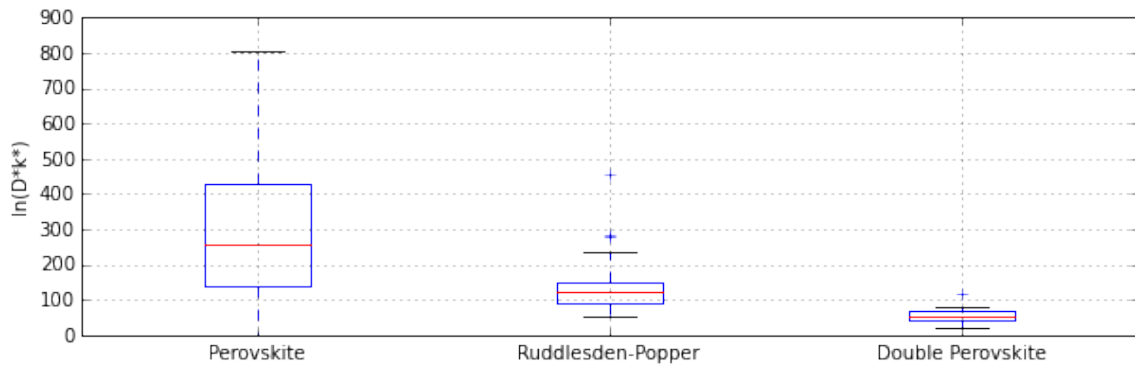


Figure 10: Box plots of material family vs $\ln(D \cdot k^*)$ at 700K

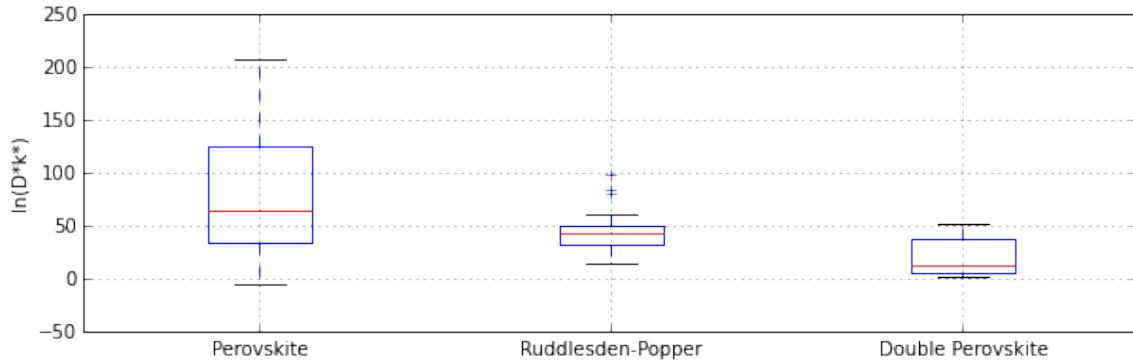


Figure 11: Box plots of material family vs $\ln(D \cdot k^*)$ at 1000K

Three separate ANOVA tests were performed: one for each of the three categorical variables (material family, sample type, and measurement type) explored in this analysis. P-values, that is, the probability that the subgroups are not significantly different from one another⁷, are summarized in Table 2.

T(K)	Material Family	Sample Type	Measurement Type
400	$8.37 \cdot 10^{-7}$	0.022	0.182
700	$4.88 \cdot 10^{-7}$	0.013	0.156
1000	$3.13 \cdot 10^{-6}$	0.008	0.105

Table 2: p-values of ANOVAs corresponding to $\ln(D \cdot k^*)$

The data show that any given material's measured value of $\ln(D \cdot k^*)$ (and thus its ion diffusion rate) depends on material family, i.e. whether the material is perovskite, Ruddlesden-Popper, or double perovskite. This means material family has a statistically

⁷ Significance is defined by a test resulting in a p-value less than 0.05.

significant effect on ion diffusion rate. Similarly, a material will show significantly different diffusion depending on the type of sample measured, i.e. whether it was ceramic, single crystal, or thin film. Conversely, the method used to measure the sample (IEDP/SIMS, ECR, etc.) does not have a significant effect on the diffusion rate.

3.3 PREDICTIVE ANALYSIS

An analysis was performed to determine which feature (or features) in Table 1 explained the most variation in $\ln(D \cdot k^*)$. Because experimental data were used (rather than theoretical data), the analysis was limited to atomic-scale quantitative features derived from chemical formula and crystal structure. Categorical features, e.g. sample type, have no numerical values and were also used.

3.3.1 The Initial Model

Since most experiments in the literature were conducted near the high temperature limit of the analysis (1000K), this was the temperature used to build the initial model. This model was built for perovskites and double perovskites, as they made up the bulk of the data.

Selecting a feature subset: Recursive feature elimination was used with a linear regularized regression to rank the amount of variation explained by each individual feature (Table 3).

Feature	RFE Rank
Electron Affinity (B-site, average)	1
Radius (B-site, parent)	2
Radius (B-site, average)	3
Tolerance Factor	4
Electron Affinity (B-sit, parent)	5
d count (B-site, average)	6
d count (B-site, parent)	7
Critical Radius	8
Electron Affinity (A-site, parent)	9
Electron Affinity (A-site, average)	10
Radius (A-site, parent)	11
Radius (A-site, average)	12

Table 3: Recursive Feature Elimination (RFE) results

B-site features were more predictive of fast ion transport than A-site features. Of the B-site features, average ones were generally more predictive than parent ones (see Section 2.2.4). Scatter plots were drawn to visually inspect differences in parent and average features (Figures 12-14). Both feature classes followed the same trends, but the average features showed much more information about the shapes of these functions.

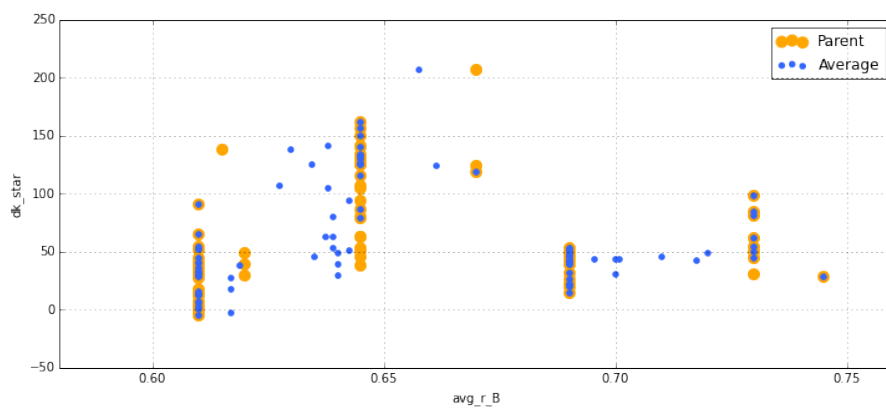


Figure 12: Ionic radius (B-cation) vs $\ln(D \cdot k^*)$

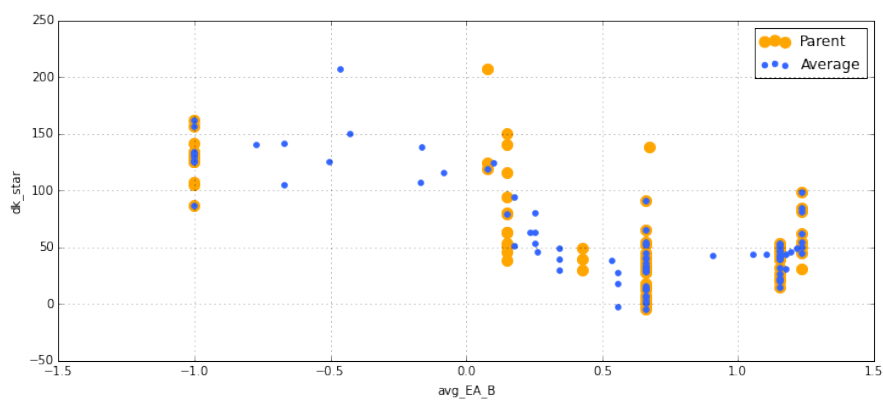


Figure 13: Electron Affinity (B-cation) vs $\ln(D \cdot k^*)$

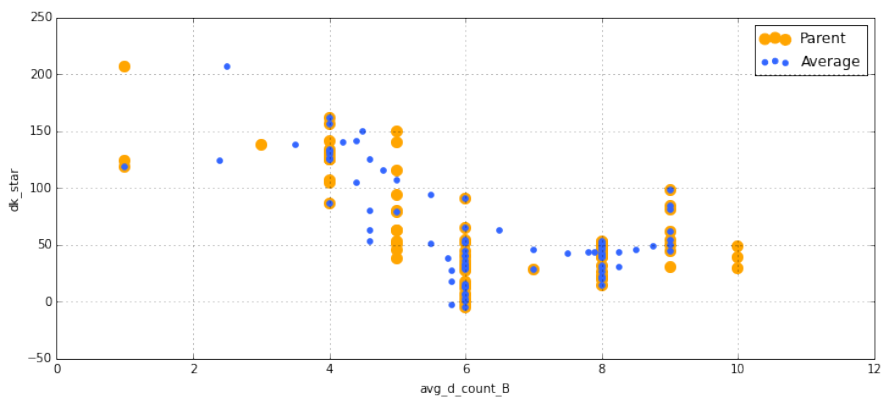


Figure 14: d electron count (B-cation) vs $\ln(D \cdot k^*)$

Separate regularized polynomial regression models were created for parent and average feature sets. The models were both optimized to fifth order functions after 50 iterations of leave-one-out cross validation. The mean squared error (MSE) for the parent features model was 611.6. The MSE for the average features model was 372.9. This suggested average features were superior for use in modeling.

Principle Component Analysis (PCA) was performed with the average features to determine how much variance was captured by the first principle component and, subsequently, by the individual features that were projected onto that component. PCA showed that the first component corresponded to an eigenvector of 0.945 meaning almost 95% of the variation was captured by the first component alone. Table 4 shows coefficients corresponding to projections of the individual features onto the first principle component.

Feature	Coefficient
d count (B-site, average)	0.941
Electron Affinity (B-site, average)	0.331
Radius (B-site, average)	0.013
Tolerance Factor	0.019
Critical Radius	0.028
Electron Affinity (A-site, average)	0.040
Radius (A-site, average)	0.040

Table 4: Feature projections onto the first principle component

Only two features had projection coefficients greater than 0.04: electron affinity of the B-site cation and d electron count of the B-site cation. It was expected that at least one of these would be used in the ensuing model.

Building the model: A polynomial, regularized regression was used to build a model from a subset of average features. Features were added to the model one at a time. The feature resulting in the lowest mean squared error (MSE) given the existing features was added to the model, but only if it decreased MSE by >5% (to avoid overfitting). Electron affinity of the B-site cation had the lowest MSE (881.5) so it was included in the model. The next best feature was average d electron count of the B-cation, but it only decreased MSE by 4.5% and was therefore left out. No other quantitative features decreased MSE by a significant amount.

Categorical features were also analyzed. Measurement type only decreased MSE by a trivial amount (0.7%), so it was left out. Material family and sample type reduced MSE by 8.3% and 6.9%, respectively and were both included.

3.3.2 Recreating the Model at Other Temperatures

Models were built with the same features using $\ln(D^*k^*)$ values calculated at 400K, 500K, 600K, 700K, 800K, 900K, and 1000K. Note that D^*k^* depends on temperature, but none of the features do.

Perovskite and Double Perovskite Models: The resulting models were first order polynomial functions (with respect to B-cation electron affinity) at low temperatures and higher order polynomials at higher temperatures (Table 5). However, the higher order models were heavily regularized and still maintained roughly linear shapes (Figure 9). Models fit at low temperatures were much less accurate (i.e. had higher MSE) than models at high temperatures. Most of the data came from perovskites studied at high temperatures, so a large percentage of the data was extrapolated to lower temperatures using Arrhenius behavior. As discussed earlier, it is often a dubious assumption to extrapolate Arrhenius behavior too far from the measured temperature. Nevertheless, all models follow the same trend.

Temperature (K)	Polynomial Order	Mean Squared Error
400	1	377069.1
500	1	99360.0
600	1	29912.4
700	1	9917.0
800	3	3490.3
900	5	1366.5
1000	5	654.7

Table 5: Model error at multiple temperatures

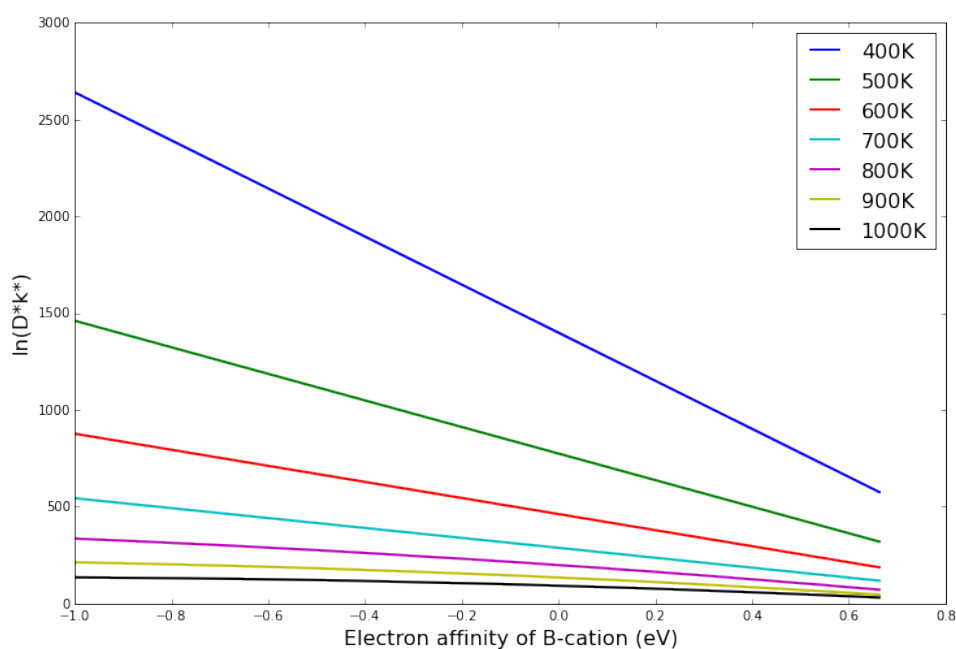


Figure 15: Electron affinity vs $\ln(D^*k^*)$ – Perovskite and Double Perovskite

Goodness of model fit was evaluated using the coefficient of determination, R^2 (Figure 10). Models above 700K explained more than 85% of the variance, meaning

these models successfully predicted $\ln(D^*k^*)$ more than 85% of the time. Models at lower temperatures only explained 55-70%. This difference is likely a result of extrapolation error.

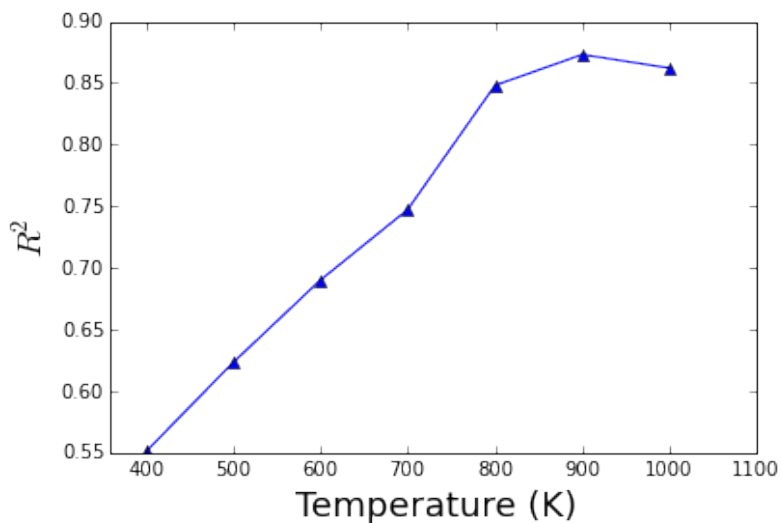


Figure 16: Variation in $\ln(D^*k^*)$ captured by Perovskite and Double Perovskite models

Ruddlesden-Popper Models: Fewer than 20 data points were available for Ruddlesden-Popper materials. The best feature to add was average d electron count of the B-site cation, with a model MSE of 193.6. A second feature was added (average electron affinity of the A-site cation), which decreased the MSE by 12%. MSE values for Ruddlesden-Popper models were significantly lower at all temperatures than they were for the corresponding perovskite/double perovskite models. However, Ruddlesden-

Popper models were highly overfit and showed no trends. Thus, overfitting could not be remedied by leave-one-out cross-validation and it was determined no generalizable model could be created out of the few Ruddlesden-Popper data points that were available.

Chapter 4: Conclusions

Three material families (perovskites, Ruddlesden-Popper phases, and double perovskites) were explored to determine what atom-scale features could be used to predict fast ion diffusion for Solid Oxide Fuel Cells at intermediate and low temperatures. ANOVA tests revealed that these three families of materials showed significant differences in oxide diffusion rates, indicated by $\ln(D \cdot k^*)$. Perovskites, on average, showed the slowest diffusion at all temperatures. Ruddlesden-Popper materials showed slightly faster diffusion on average. Diffusion was fastest in double perovskites. This suggests layered perovskites do indeed exhibit faster ion diffusion on average than bulk perovskites and hence that MIEC cathodes are a feasible way to lower the operating temperatures of SOFCs.

Models were constructed from subsets of 13 features that described various structural or chemical features. Because perovskites and double perovskites exhibit vacancy diffusion, a common model could be constructed from both sets of data. Ruddlesden-Popper materials exhibit oxide diffusion via interstitial migration so a separate model was required. Unfortunately, not enough data was available to create a generalizable model for Ruddlesden-Popper materials.

In perovskites and double perovskites, ion transport occurs by a vacancy-assisted mechanism. When a vacancy forms, the neighboring B-site cations are reduced. The energetic propensity for this reduction may be captured by the electron affinity of the B-site cation (an atomic property). In the models created here, oxide diffusion is most

strongly correlated to this property; higher electron affinity corresponds to faster diffusion at all temperatures. This suggests using B-site cations with higher electron affinities has a positive effect on SOFC performance.

Cathode materials are important to the overall performance of the Solid Oxide Fuel Cell. Layered perovskites show the promise of exhibiting faster diffusion than bulk perovskites at all temperatures. More research is needed on layered perovskites to determine their commercial viabilities, but this analysis concludes that selecting conventional perovskites with higher B-site electron affinities could benefit fuel cells that are currently being built.

References:

- [1] Johnston, Simon, et al. "Science with the Australian square kilometre array pathfinder." *Publications of the Astronomical Society of Australia* 24.04 (2007): 174-188.
- [2] Kim, Junsung, et al. "Parallel scheduling for cyber-physical systems: Analysis and case study on a self-driving car." *Proceedings of the ACM/IEEE 4th International Conference on Cyber-Physical Systems*. ACM, 2013.
- [3] Gaultois, Michael W., et al. "Data-driven review of thermoelectric materials: performance and resource considerations." *Chemistry of Materials* 25.15 (2013): 2911-2920.
- [4] Balachandran, Prasanna V., and James M. Rondinelli. "Interplay of octahedral rotations and breathing distortions in charge-ordering perovskite oxides." *Physical Review B* 88.5 (2013): 054101.
- [5] Owen, Anthony D. "Renewable energy: Externality costs as market barriers." *Energy Policy* 34 (2006) 632-642.
- [6] Blanco, Maria I. "The economics of wind energy." *Renewable and Sustainable Energy Reviews* 13 (2009) 137201382.
- [7] "How We Use Energy, Transportation." *The National Academics*.
<http://needtoknow.nas.edu/energy/energy-use/transportation/>
- [8] Andersen, Poul H., John A. Mathews, and Morten Rask. "Integrating private transport into renewable energy policy: The strategy of creating intelligent recharging grids for electric vehicles." *Energy Policy* 37.7 (2009): 2481-2486.
- [9] Zhu, Huayang, and Robert J. Kee. "Thermodynamics of SOFC efficiency and fuel utilization as functions of fuel mixtures and operating conditions." *Journal of Power sources* 161.2 (2006): 957-964.
- [10] Stambouli, A. Boudghene, and E Traversa. "Solid oxide fuel cells (SOFCs): a review of an environmentally clean and efficient source of energy." *Renewable and Sustainable Energy Reviews* 6, no. 5 (October 2002): 433-55.

- [11] Carrette, L., K. A. Friedrich, and U1 Stimming. "Fuel cells—fundamentals and applications." *Fuel cells* 1.1 (2001): 5-39.
- [12] Park, Seungdo, John M. Vohs, and Raymond J. Gorte. "Direct oxidation of hydrocarbons in a solid-oxide fuel cell." *Nature* 404.6775 (2000): 265-267.
- [13] Ormerod, R. Mark. "Solid oxide fuel cells." *Chemical Society Reviews* 32.1 (2003): 17-28.
- [14] Brett, Daniel JL, et al. "Intermediate temperature solid oxide fuel cells." *Chemical Society Reviews* 37.8 (2008): 1568-1578.
- [15] Tarancón, Albert, Stephen J. Skinner, Richard J. Chater, F. Hernández-Ramírez, and John A. Kilner. Layered perovskites as promising cathodes for intermediate temperature solid oxide fuel cells. *Journal of Materials Chemistry* 17.30 (2007): 3175.
- [16] Kuklja, M. M., E. A. Kotomin, R. Merkle, Yu. A. Mastrikov, and J. Maier. Combined theoretical and experimental analysis of processes determining cathode performance in solid oxide fuel cells. *Physical Chemistry Chemical Physics* 15.15 (2013): 5443.
- [17] Mastrikov, Yuri A., et al. "Pathways for oxygen incorporation in mixed conducting perovskites: A DFT-based mechanistic analysis for (La, Sr) MnO_{3-δ}." *The Journal of Physical Chemistry C* 114.7 (2010): 3017-3027.
- [18] Cherry, M., M.S. Islam, and C.R.A. Catlow. Oxygen Ion Migration in Perovskite-Type Oxides. *Journal of Solid State Chemistry* 118.1 (1995): 125-32.
- [19] Sundell, Per G., Mårten E. Björketun, and Göran Wahnström. "Thermodynamics of doping and vacancy formation in BaZrO₃ perovskite oxide from density functional calculations." *Physical Review B* 73.10 (2006): 104112.
- [20] Islam, M. S., M. Cherry, and C. R. A. Catlow. "Oxygen diffusion in LaMnO₃ and LaCoO₃ perovskite-type oxides: a molecular dynamics study." *Journal of Solid State Chemistry* 124.2 (1996): 230-237.

- [21] Goldschmidt, Victor Moritz. "Die gesetze der krystallochemie." *Naturwissenschaften* 14.21 (1926): 477-485.
- [22] Shiiba, Hiromasa, Clare L. Bishop, Michael J. D. Rushton, Masanobu Nakayama, Masayuki Nogami, John A. Kilner, and Robin W. Grimes. Effect of A-site cation disorder on oxygen diffusion in perovskite-type $\text{Ba}_{0.5}\text{Sr}_{0.5}\text{Co}_{(1-x)}\text{Fe}_x\text{O}_3$. *Journal of Materials Chemistry A* 1.35 (2013): 10345.
- [23] Kotomin, E.A., Yu. A. Mastrikov, M.M. Kuklja, R. Merkle, A. Roytburd, and J. Maier. First principles calculations of oxygen vacancy formation and migration in mixed conducting $\text{Ba}_{0.5}\text{Sr}_{0.5}\text{Co}_{(1-y)}\text{Fe}_y\text{O}_3$ perovskites. *Solid State Ionics* 188.1 (2011): 1-5.
- [24] IUPAC, *Compendium of Chemical Terminology*, 2nd ed. (the "Gold Book") (1997). Online corrected version: (2006–) "Electron affinity".
- [25] R. Cook and A. Sammels. On the systematic selection of perovskite solid electrolytes for intermediate temperature fuel cells. *Solid State Ionics* 45.3-4 (1991): 311-21.
- [26] Xu, Nansheng, Hailei Zhao, Xiong Zhou, Wenjing Wei, Xionggang Lu, Weizhong Ding, and Fushen Li. Dependence of critical radius of the cubic perovskite ABO_3 oxides on the radius of A- and B-site cations. *International Journal of Hydrogen Energy* 35.14 (2010): 7295-1.
- [27] Munnings, C. N., et al. "Oxygen transport in the $\text{La}_{2-x}\text{Ni}_{1-x}\text{Co}_x\text{O}_{4+\delta}$ system." *Solid State Ionics* 176.23 (2005): 1895-1901.
- [28] Allan, N. L., and W. C. Mackrodt. "Oxygen ion migration in La_2CuO_4 ." *Philosophical Magazine A* 64.5 (1991): 1129-1132.
- [29] Parfitt, David, Alexander Chroneos, John A. Kilner, and Robin W. Grimes. Molecular dynamics study of oxygen diffusion in $\text{Pr}_2\text{NiO}_{(4+\delta)}$. *Physical Chemistry Chemical Physics* 12.25 (2010): 6834.
- [30] Taskin, A. A., A. N. Lavrov, and Yoichi Ando. Achieving fast oxygen diffusion in perovskites by cation ordering. *Applied Physics Letters* 86.9 (2005): 091910.

- [31] Kim, G., S. Wang, A. J. Jacobson, L. Reimus, P. Brodersen, and C. A. Mims. Rapid oxygen ion diffusion and surface exchange kinetics in $\text{PrBaCo}_2\text{O}_{(5+x)}$ with a perovskite related structure and ordered A cations. *Journal of Materials Chemistry* 17.24 (2007): 2500.
- [32] Kubicek, Markus, Zhuhua Cai, Wen Ma, Bilge Yildiz, Herbert Hutter, and Jürgen Fleig. Tensile Lattice Strain Accelerates Oxygen Surface Exchange and Diffusion in La. *ACS Nano* 7.4 (2013): 3276-86.
- [33] Wang, L., R. Merkle, J. Maier, T. Acartürk, and U. Starke. Oxygen tracer diffusion in dense $\text{Ba}_{0.5}\text{Sr}_{0.5}\text{Co}_{0.8}\text{Fe}_{0.2}\text{O}_3$ films. *Applied Physics Letters* 94.7 (2009): 071908.
- [34] Claus, Jürgen, Günter Borchardt, Sylvain Weber, Jean-Marie Hiver, and Stanislas Scherrer. Combination of EBSD measurements and SIMS to study crystallographic orientation dependence of diffusivities in a polycrystalline material: oxygen tracer diffusion in $\text{La}_{(2-x)}\text{Sr}_x\text{CuO}_{4+y}$ *Materials Science and Engineering: B* 38.3 (1996): 251-57.
- [35] Bassat, J. Anisotropic ionic transport properties in $\text{La}_2\text{NiO}_{(4+\delta)}$ single crystals. *Solid State Ionics* 167.3-4 (2004): 341-47.
- [36] Burriel, Monica, Gemma Garcia, Jose Santiso, John A. Kilner, Richard J. Chater, and Stephen J. Skinner. Anisotropic oxygen diffusion properties in epitaxial thin films of $\text{La}_2\text{NiO}_{(\delta\delta\delta)}$. *J. Mater. Chem.* 18.4 (2008): 416-22.
- [37] Taskin, A.A., A.N. Lavrov, and Yoichi Ando. Fast oxygen diffusion in A-site ordered perovskites. *Progress in Solid State Chemistry* 35.2-4 (2007): 481-90.
- [38] Zhang, Kun, Lei Ge, Ran Ran, Zongping Shao, and Shaomin Liu. Synthesis, characterization and evaluation of cation-ordered $\text{LnBaCo}_2\text{O}_{(5+x)}$ as materials of oxygen permeation membranes and cathodes of SOFCs. *Acta Materialia* 56.17 (2008): 4876-89.
- [39] Fischer, Eric, and Joshua L. Hertz. Measurability of the diffusion and surface exchange coefficients using isotope exchange with thin film and traditional samples. *Solid State Ionics* 218 (2012): 18-24.
- [40] Kilner, John A., Stephen J. Skinner, and Hidde H. Brongersma. The isotope exchange depth profiling (IEDP) technique using SIMS and LEIS. *Journal of Solid State Electrochemistry* 15.5 (2011): 861-76.

- [41] Li, Yihong, Kirk Gerdes, Harvey Diamond, and Xingbo Liu. An improved method to increase the predictive accuracy of the ECR technique. *Solid State Ionics* 204-205 (2011): 104-10.
- [42] De Souza, R. A. A universal empirical expression for the isotope surface exchange coefficients (k^*) of acceptor-doped perovskite and fluorite oxides. *Physical Chemistry Chemical Physics* 8.7 (2006): 890.
- [43] Armstrong, Eric N., Keith L. Duncan, and Eric D. Wachsman. Effect of A and B-site cations on surface exchange coefficient for ABO_3 perovskite materials. *Physical Chemistry Chemical Physics* 15.7 (2013): 2298.
- [44] Jones, Eric, Travis Oliphant, and Pearu Peterson. "{SciPy}: Open source scientific tools for {Python}." (2014).
- [45] Wes McKinney. Data Structures for Statistical Computing in Python, Proceedings of the 9th Python in Science Conference, 51-56 (2010)
- [46] Fabian Pedregosa, Gaël Varoquaux, Alexandre Gramfort, Vincent Michel, Bertrand Thirion, Olivier Grisel, Mathieu Blondel, Peter Prettenhofer, Ron Weiss, Vincent Dubourg, Jake Vanderplas, Alexandre Passos, David Cournapeau, Matthieu Brucher, Matthieu Perrot, Édouard Duchesnay. Scikit-learn: Machine Learning in Python, *Journal of Machine Learning Research*, 12, 2825-2830 (2011)
- [47] Fisher, Ronald A. "The use of multiple measurements in taxonomic problems." *Annals of eugenics* 7.2 (1936): 179-188.
- [48] Weisstein, Eric W. "L2-Norm." From MathWorld--A Wolfram Web Resource.
<http://mathworld.wolfram.com/L2-Norm.html>
- [49] Weisstein, Eric W. "L1-Norm." From MathWorld--A Wolfram Web Resource.
<http://mathworld.wolfram.com/L1-Norm.html>
- [50] Reineking, Björn. "Constrain to perform: regularization of habitat models." *Ecological Modelling* 193.3 (2006): 675-690.
- [51] What is Distributed Generation? Bloom Energy website <http://www.bloomenergy.com/fuel-cell/distributed-generation/>. Updated 2014.

- [52] Reliable Power for Mission Critical Systems. Bloom Energy website
<http://www.bloomenergy.com/fuel-cell/mission-critical-data-center/>. Updated 2014.
- [53] Boehm, Emmanuelle, et al. "Oxygen diffusion and transport properties in non-stoichiometric Ln_{2-x}NiO_{4+δ} oxides." *Solid State Ionics* 176.37 (2005): 2717-2725.
- [54] Adler, Stuart B. "Factors governing oxygen reduction in solid oxide fuel cell cathodes." *Chemical reviews* 104.10 (2004): 4791-4844.
- [55] Chen, Yi-Ching, et al. "Crystal Structure, Oxygen Deficiency, and Oxygen Diffusion Path of Perovskite-Type Lanthanum Cobaltites La_{0.4}Ba_{0.6}CoO_{3-δ} and La_{0.6}Sr_{0.4}CoO_{3-δ}." *The Journal of Physical Chemistry C* 116.8 (2012): 5246-5254.
- [56] Mastrikov, Yuri A., et al. "Formation and migration of oxygen vacancies in La_{1-x}Sr_xCo_{1-y}Fe_yO_{3-δ} perovskites: insight from ab initio calculations and comparison with Ba_{1-x}Sr_xCo_{1-y}Fe_yO_{3-δ}." *Physical chemistry chemical physics* 15.3 (2013): 911-918.
- [57] Ishihara, Tatsumi, Hideaki Matsuda, and Yusaku Takita. "Doped LaGaO₃ perovskite type oxide as a new oxide ionic conductor." *Journal of the American chemical society* 116.9 (1994): 3801-3803.
- [58] Allen, David M. "Mean square error of prediction as a criterion for selecting variables." *Technometrics* 13.3 (1971): 469-475.
- [59] Menard, Scott. "Coefficients of determination for multiple logistic regression analysis." *The American Statistician* 54.1 (2000): 17-24.
- [60] Wold, Svante, Kim Esbensen, and Paul Geladi. "Principal component analysis." *Chemometrics and intelligent laboratory systems* 2.1 (1987): 37-52.
- [61] Yeh, Ted C., Jules L. Routbort, and Thomas O. Mason. "Oxygen transport and surface exchange properties of Sr_{0.5}Sm_{0.5}CoO_{3-δ}." *Solid State Ionics* 232 (2013): 138-143.
- [62] Mauvy, F., J.M. Bassat, E. Boehm, P. Dordor, J.C. Grenier, and J.P. Loup. Chemical oxygen diffusion coefficient measurement by conductivity relaxation: correlation between tracer diffusion coefficient and chemical diffusion coefficient. *Journal of the European Ceramic Society* 24.6 (2004): 1265-69.

[63] Schlom, Darrell G., et al. "A thin film approach to engineering functionality into oxides." *Journal of the American Ceramic Society* 91.8 (2008): 2429-2454.

[64] Minervini, Licia, et al. "Oxygen migration in $\text{La}_2\text{NiO}_{4+\delta}$." *Journal of Materials Chemistry* 10.10 (2000): 2349-2354.

[65] Amow, G., and S. J. Skinner. "Recent developments in Ruddlesden–Popper nickelate systems for solid oxide fuel cell cathodes." *Journal of Solid State Electrochemistry* 10.8 (2006): 538-546.

[66] Vert, Vicente B., et al. "Enhanced oxygen diffusion in low barium-containing $\text{La}_{0.2175}\text{Pr}_{0.2175}\text{Ba}_{0.145}\text{Sr}_{0.4}\text{Fe}_{0.8}\text{Co}_{0.2}\text{O}_{3-\delta}$ intermediate temperature solid oxide fuel cell cathodes." *Journal of Power Sources* 213 (2012): 270-274.

[67] Kim, Guntae, et al. "Measurement of oxygen transport kinetics in epitaxial $\text{La}_2\text{NiO}_{4+\delta}$ thin films by electrical conductivity relaxation." *Solid State Ionics* 177.17 (2006): 1461-1467.